Tomography-Based Heat And Mass Transport Characterization Of Complex Porous Materials For Solar Power And Fuel Generation

S. Haussener[1, 2], A. Steinfeld[3, 4]

[1]*Department of Mechanical Engineering, EPFL, 1015 Lausanne, Switzerland*
[2]*Lawrence Berkeley National Laboratory, Berkeley, CA 94720, USA*
[3]*Departement of Mechanical and Process Engineering, ETH, 8092 Zurich, Switzerland*
[4]*Solar Technology Laboratory, Paul Scherrer Institute, 5232 Villigen, Switzerland*

Abstract: Transport phenomena in porous media are pertinent to thermal and thermochemical processes for power and fuel generation using concentrated solar energy. The porous media serve as insulator, radiant absorbers, heat exchangers, catalyst carriers, reactants, and/or reaction sites. Volume-averaging models for porous media, commonly applied for process simulations and optimization, rely heavily on the a-priori determination of their effective transport properties, which in turn depend strongly on the morphology of the porous media.

A combined experimental-numerical methodology is applied to accurately determine these effective properties. The exact 3D geometrical structure is obtained by computed tomography and applied in subsequent direct pore-level numerical simulations of heat and mass transfer using Monte Carlo and finite volume techniques. Three examples of materials widely used in solar applications are selected: (*i*) a reacting packed bed of carbonaceous materials undergoing solar-driven gasification; (*ii*) a ceramic foam for a solar pressurized air receiver coupled to a gas turbine; and (*iii*) an anisotropic ceramic foam for a solar H_2O/CO_2-splitting thermochemical cycle. A comprehensive characterization of morphology and heat/mass transport properties is accomplished via Monte Carlo and finite volume techniques.

Keywords: Solar fuels, solar materials, concentrating solar power, porous media, effective transport properties.

1. Introduction

We consider solar thermal and thermochemical processes to generate electricity and (storable) chemical fuels [1]. In these processes, porous media serve as insulators, radiant absorbers, heat exchanges, catalyst carriers, reactants, and reaction sites. The analysis of the interactions between multi-mode heat transfer, multiphase flow, and chemical reaction on multiple scales is fundamental for understanding and optimizing these processes, but it is challenging because of the porous media's inherent structural complexity and scale disparity. Therefore, multi-scale approaches using averaging procedures have been introduced [2]. Essentially, conservation equations valid in each continuous phase are spatially smoothed and effective transport properties are introduced to produce equations that are valid throughout the porous media. These properties are strongly dependent on the phase boundaries and, consequently, on the morphology, and are among the most sensitive parameters in volume-averaged models.

Sophia Haussener, sophia.haussener@epfl.ch

A wide range of semi-empirical correlations for the effective heat and mass transport properties have been developed based on experimental fits and on simplified geometries. Previous pertinent studies on effective transport properties of foams and packed beds include the determination of the extinction coefficient, scattering coefficient, and scattering phase function for simplified geometries composed of pentagon dodecahedron or tetracaedecaedric [3], spherical voided cubic unit cells [4] and overlapping spheres [5-7]. The effective thermal conductivity has been determined for simplified geometries composed of tetrakaidecahedron [8], hexagonal [9], and spherical or cubical voided cubic unit cells [10]. Permeability has been determined by simplifying the foam or packed bed structure by parallel conduits [11]. Spectroscopy measurements were used for the determination of effective extinction coefficients, scattering coefficients and phase functions of foams and packed beds [12,13]. A steady-state radial heat flow setup was used for the determination of the effective conductivity of complex packed beds [14]. Correlations based on experimental conduction and convection were derived for alumina foams in water and air [15] and for foams and packed beds composed of spherical or non-spherical particles [16-18]. Similarly, permeability and Dupuit-Forchheimer coefficient were determined based on semi-empirical models such as capillary or hydraulic radius models and Ergun's model [19,20].

A combined experimental-numerical procedure is adopted in this paper. The exact 3D geometry of the complex porous media determined by computed tomography is employed in direct pore-level numerical simulations for the morphological characterization and determination of the effective heat and mass transport properties [21,22]. Two-point correlation functions and mathematical morphology operations [23] are applied for the morphological characterization. Collision-based Monte Carlo is applied to calculate distribution functions of attenuation path length and direction of incidence at the phase boundary which are used to determine effective radiative properties [5]. Experimental validation is accomplished by spectroscopic measurements. Finite volume techniques are applied to solve the mass, momentum and energy conservation equations for the conductive/convective heat transfer and flow characterization [13].

A short introduction to volume averaging theory and the CT-based methodology is given in section 2. The methodology used to obtain the exact 3D geometry is described in section 3. The methodology is then applied to three examples of multi-phase media relevant in solar power generation and fuel processing: (i) reacting packed beds, (ii) porous ceramics and (iii) anisotropic ceramic foams.

2. Governing equations and methodology

2.1. Definitions and assumptions

The scalar quantity ψ_i for phase i can be expressed as summation of its average and its fluctuation,

$$\psi_i = \langle \psi_i \rangle + \psi_i',$$

(1)

where the superficial average is given by an integration over a representative volume V,

$$\langle \psi_i \rangle = \frac{1}{V} \int_V \psi_i \mathrm{d}V.$$

(2)

The spatial averaging theorem relates the superficial average of the gradient of ψ_i to the gradient of its average by

$$\langle \nabla \psi_i \rangle = \nabla \langle \psi_i \rangle - \frac{1}{V} \sum_{j=1}^{N_i} \int_{A_{ij}} \psi_i \hat{\mathbf{n}}_{ji} \mathrm{d}A,$$

where A_{ij} is the phase boundary between phase i and j.

(3)

The averaging volume V is assumed to be sufficiently large to include all typical morphological structures of the multi-component medium and sufficiently small as compared to the overall size of the multi-component medium so that $\langle \psi_i \rangle$ and $\langle \nabla \psi_i \rangle$ are assumed to be continuous scalar and vector fields, respectively.

2.2. Heat transfer

The discrete-scale energy equations for each phase are spatially averaged resulting in continuum-scale energy equations valid for the different phases. The resulting equations are closed by effective heat transfer properties such as effective conductivity, k_e, when applying the 1-equation averaging model [2], and effective heat transfer coefficient, h_e, yielding

$$(\rho c_p)_f \left[\frac{\partial \langle T_f \rangle}{\partial t} + \nabla \langle \mathbf{u}_f T_f \rangle \right] = \nabla \cdot (k_e \langle T_f \rangle^f) - h_e A_{sf}(\langle T_s \rangle^s - \langle T_f \rangle^f) - \langle \nabla \mathbf{q}''_{r,f} \rangle + \langle q'''_f \rangle , \tag{4}$$

for the fluid phase of a two-phase (solid-fluid) media. For non-negligible radiative heat transfer, additionally, effective extinction coefficients, β, scattering coefficients, σ_s, and scattering phase functions, Φ, are introduced and used for the determination of the averaged radiative flux term present in the averaged energy equation. Detailed derivation of the radiative contribution by means of averaging of the radiative transfer equations (RTE) are given in [24]. The resulting averaged RTEs for a two-phase media composed of two semitransparent phases is given by

$$\hat{\mathbf{s}} \cdot \nabla I_i(\mathbf{x}, \hat{\mathbf{s}}) = -\beta_i I_i(\mathbf{x}, \hat{\mathbf{s}}) + \kappa_{d,i} I_{b,i}(\mathbf{x}, \hat{\mathbf{s}}) + \frac{\sigma_{s,ii}}{4\pi} \int_{\Omega_i=0}^{4\pi} I_i(\mathbf{x}, \hat{\mathbf{s}}_i) \Phi_{ii}(\hat{\mathbf{s}}_i, \hat{\mathbf{s}}) \, d\Omega_i$$

$$+ \frac{\sigma_{s,ji}}{4\pi} \int_{\Omega_i=0}^{4\pi} I_j(\mathbf{x}, \hat{\mathbf{s}}_i) \Phi_{ji}(\hat{\mathbf{s}}_i, \hat{\mathbf{s}}) \, d\Omega_i , \qquad i,j = 1,2; i \neq j \tag{5}$$

where I is the superficial average of the discrete-scale intensity.

The effective radiative properties of the porous sample are determined by a collision-based Monte Carlo (MC) method, which calculates the discrete-scale distribution functions of attenuation path lengths and angle of surface incidence for each phase [5,25], which are directly related to β, σ_s, and Φ.

k_e is calculated by finite volume (FV) technique, which is used to solve the discrete-scale steady state energy equations for each phase in a 1D situation [21,22] obtained by solving the equations for a representative cubic sample with given inlet and outlet temperatures (T_1, T_2) and adiabatic lateral walls. The resulting quasi 1D heat flux,

$$\langle q'' \rangle = \frac{-\int_{A_s} k_s \nabla T_s \cdot \hat{\mathbf{n}} dA_s - \int_{A_f} k_f \nabla T_f \cdot \hat{\mathbf{n}} dA_f}{A_s + A_f} , \tag{6}$$

can be related to k_e by

$$\langle q'' \rangle = k_e \frac{T_1 - T_2}{l} , \tag{7}$$

where k_f and k_s are the discrete-scale conductivities of the fluid and solid phase, and A_f and A_s the projected surface area of the fluid and the solid phase.

Unstructured tetrahedral computational grids are commonly used for the complex morphologies of porous media, exemplary depicted in Fig.1 by a surface rendering of the 3D grid.

h_e is calculated by FV technique, which is used to solve the mass, momentum and energy equations in the fluid phase of a representative volume of the porous sample with the appropriate boundary conditions. The inter-phase heat transfer is directly related to the effective heat transfer coefficient [21,22].
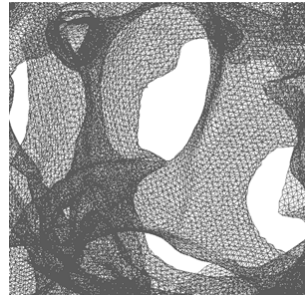

Fig. 1. Surface rendering of an unstructured tetrahedral grid of a ceramic foam.

2.3. Mass transfer

The averaging of the pore-level momentum equation results in Darcy's equation with the Dupuit-Forchheimer extension [26]. The effective mass transfer properties, i.e. permeability K and Dupuit-Forchheimer coefficient F_{DF}, are determined by solving the discrete-scale mass and momentum equations in the fluid phase of the representative volume of the porous sample followed by the calculation of the Re-dependent pressure drop in the sample, which is directly related to K and F_{DF}. Additionally, dispersion tensor, tortuosity and residence time distributions can be calculated based on the calculated discrete-scale velocity field [22].

3. Morphological characterization

The derivation of the governing equations introduced in section 2 show that the effective transport properties strongly depend on the sample's morphology. Computed tomography (CT) is used to experimentally obtain the exact discrete-scale geometry to be incorporated in the subsequent discrete-scale numerical calculations of the morphological, effective heat [21,22,27] and mass [21,22,28,29] transport properties of foams, fibers and packed beds.

3.1. Computed tomography

CT uses multiple 2D projections of an object to reconstruct its complete internal structure. Mathematical methods such as inverse Radon transform are used, in which the intensity data acquired by a detector at multiple tilt angles are used to determine the spatial (2D or 3D) distribution of the measured property. Attenuation, phase contrast or diffraction mode are used to inversely determine the distribution of the absorption coefficient, refractive index, and apparent scattering coefficient within the sample. Tomography techniques are classified according to the physical mechanism used as a source of the 2D projections, determining the size and resolution of the scans.

3.2. Digitalization

The data obtained by CT consists of 2 byte optical density values arranged on a 3D Cartesian grid. Multi-phase media are composed of different regions, each with a comparatively uniform optical density. These different regions, called phases, reflect the different components present within the material. In order to digitalize the geometry and to process with numerical calculations, these phases must be identified, thereby partitioning the grey-scale image into disjoint segments. Therefore, each voxel must be assigned to one phase. This process is called segmentation. The mode method, a histogram-based technique, is a widely used technique where a threshold optical density value for fluid-solid phase assignment is determined. A continuous boundary representation is obtained by subsequent 3D linear interpolation of the optical density values.

3.3. Morphological characteristics

Statistical (correlation) functions, namely, the two-point correlation function,

$$s_2(r) = \frac{\int_V \int_{4\pi} \Psi(\mathbf{x})\Psi(\mathbf{x}+r\hat{\mathbf{s}})\,\mathrm{d}\hat{\mathbf{s}}\,\mathrm{d}\mathbf{x}}{V4\pi}, \tag{8}$$

are used for the determination of porosity, ε, and specific surface, A_0, as $s_2(0) = \varepsilon$ and $\mathrm{d}s_2/\mathrm{d}r_{r=0} = -A_0/4$ is valid [23]. Monte Carlo sampling is used for the determination of s_2 [21,22].

REV is determined by calculating morphological, heat and/or mass transfer properties for a number of subsequently growing subvolumes in the sample until the determined properties only vary within a small band. For pore- and particle-size characterization and distribution calculations, the concept of granulometry is applied [30]. It is based on mathematical morphology operations. An opening, which consists of an erosion followed by a dilation with the same structuring element, is used to calculate the pore- and particle-size distribution. For a spherical structuring element with diameter d, the distribution function is determined by

$$f(d) = -\frac{\mathrm{d}\varepsilon_{op}(d)}{\varepsilon\,\mathrm{d}d}. \tag{9}$$

4. Applications

4.1. A reacting packed bed for the solar gasification of carbonaceous materials

The solar gasification of carbonaceous materials (coal, coke, biomass, C-containing waste, etc.) for the production of syngas is obtained by an endothermic process,

$$CH_xO_yS_zN_u + (1-y)H_2O = \frac{1}{2}(x+2(1-y)-2z)H_2 + CO + zH_2S + \frac{1}{2}uN_2 \qquad (10)$$
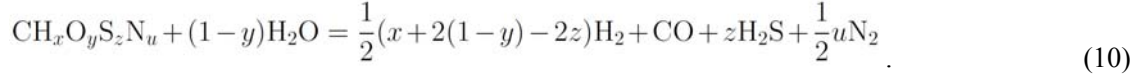
The process heat can be provided by concentrated solar energy, resulting in cleaner products since their energy content is upgraded by the solar input in amount equal to the enthalpy change of the reaction. The advantages as compared to the conventional autothermal gasification are fourfold: (i) the gaseous products are not contaminated by combustion by-products; (ii) the syngas output per unit feedstock is increased; (iii) the calorific value of the feedstock is upgraded; and (iv) the energy-intensive processing of pure oxygen is eliminated [31].
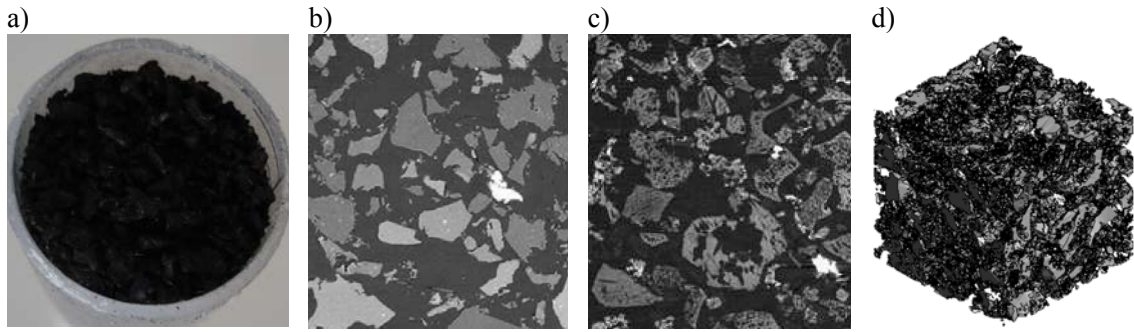
a)   b)   c)   d)

Fig. 2. Photo (a), CT image of the initial (b) and final (c) state, and 3D surface rendering of the packed bed of carbonaceous material.

Tomography-based images of the carbonaceous material (waste tire shreds, see Fig. 2a) at discrete time steps during the solar gasification reaction are used for the determination of the morphological and effective heat/mass transport properties. The CT images of the initial and final packed bed are shown in Fig. 2b and 2c and a 3D rendering of the final state is shown in Fig. 2d. The reaction conversion is characterized by the carbon conversion X_C.

Porosity calculations are fitted to a second order polynomial function

$$\varepsilon_{ex}(X_C) = -0.366X_C^2 + 0.673X_C + 0.593, \qquad (11)$$

peaking at $X_C = 0.92$ with $\varepsilon = 0.90$. Limitations in computerized tomography resolution shows to be the preliminary cause of discrepancies observed between experiments and numerical calculations, especially at larger reaction extent where nanopores are formed.

Radiative characterization obtained by the collision-based MC shows an exponential increase in the effective extinction coefficient fitted to

$$\beta_{MC}(X_C) = 3968 + 0.00138\exp(16.0X_C). \qquad (12)$$

The change is explained by the particle shrinking and break up, resulting in shorter attenuation path lengths. k_e calculated by neglecting particle-particle contact resistances decreases with reaction extent due to larger porosity and smaller particle size. The evolution of highly porous particles during pyrolysis and the subsequent shrinking and break-up of the particles cause a decrease and re-increase in convective heat exchange shown by the calculated fits given in Table 1.

The same behavior is observed for F_{DF} coefficient fitted to a function of the form

$$F_{DF}(X_C) = 75862X_C^2 - 63255X_C + 10941. \qquad (13)$$

Largest K is calculated for the highly porous particles and decreases again for the final packed bed configuration. The calculated fit is given by

$$K(X_\mathrm{C}) = -4.03 \cdot 10^{-8} X_\mathrm{C}^2 + 3.92 \cdot 10^{-8} X_\mathrm{C} + 1.24 \cdot 10^{-9}.$$ (14)

The variation of the complex morphology during the solar-driven gasification leads to significant changes in the calculated morphological and effective heat/mass transport properties and, consequently, to a more detailed knowledge of the reaction mechanism [32].

Table 1. Fitted Nu correlations for the packed bed at $X_\mathrm{C} = 0$, 0.68 and 1.

	Nu
Initial ($X_\mathrm{C} = 0$)	$8.399 + 0.234\mathrm{Re}^{0.909}\mathrm{Pr}^{0.627}$
Char ($X_\mathrm{C} = 0.68$)	$0.754 + 0.091\mathrm{Re}^{0.740}\mathrm{Pr}^{0.570}$
Ash ($X_\mathrm{C} = 1$)	$4.592 + 0.274\mathrm{Re}^{0.886}\mathrm{Pr}^{0.684}$

4.2. A ceramic foam used in solar pressurized air receivers for CSP

A solar receiver containing a ceramic foam is considered for concentrated solar power (CSP) via a Brayton cycle. The ceramic foam serves as a heat exchanger for heating pressurized air that is expanded in a gas turbine. The foam morphology (porosity, pore size distribution, isotropy etc.) influences the efficiency of the solar receiver by a great extent. Therefore, a CT-based determination of the morphological and effective heat/mass transport properties is of interest.

Exemplary, the porosity, specific surface area, and pore-size distribution of a non-hollow SiSiC reticulate porous ceramic with nominal pore diameter of 1.27 mm are calculated. A photo, CT image and 3D surface rendering of the foam are shown in Fig. 3. The CT-based methodology is used for calculating β of the foam, which equals 431 m^{-1} and compares well to experimental estimates obtained with a spectroscopy measurement setup [13]. The scattering phase function shows an enhanced fraction of backward scattering for assumed diffuse surface reflection. The ratio of effective conductivity to solid conductivity for small ratios of fluid to solid conductivities converges to 0.022. A Re and Pr dependent Nu correlation is determined and converges to 6.8 for small Re numbers. Numerically determined K and F_DF compare well to values available in literature for materials with similar morphology.
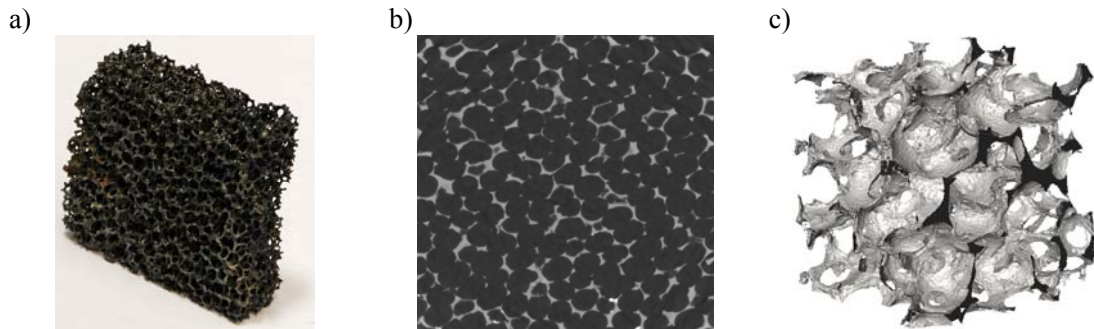
a)　　　　　　　　　　b)　　　　　　　　　　c)

Fig. 3. Photo (a), CT image (b) and 3D surface rendering of the porous ceramic sample.

Reliable determination of the effective transport properties of ceramic foams are achieved and can be extended to foams with different morphologies, allowing for optimization of solar receivers for CSP.

4.3. An anisotropic ceramic foam for a solar H$_2$O/CO$_2$-splitting thermochemical cycle

The solar production of syngas from H_2O and CO_2 via a 2-step thermochemical cycle based on ceria redox reactions is considered [33], represented by:

Reduction step (1800 K):

$$CeO_{2-\delta} = CeO_{2-\delta-x} + \frac{x}{2}O_2,$$ (15)

Oxidation step (1100 K):

$$CeO_{2-\delta-x} + xH_2O = CeO_{2-\delta} + xH_2 ,$$ (16a)

$$CeO_{2-\delta-x} + xCO_2 = CeO_{2-\delta} + xCO .$$ (16b)

Ceramic ceria foams, show in Fig. 4, with structural anisotropy due to uniaxial pressing (along the z-direction) and anisotropic primary particles are numerically analyzed.
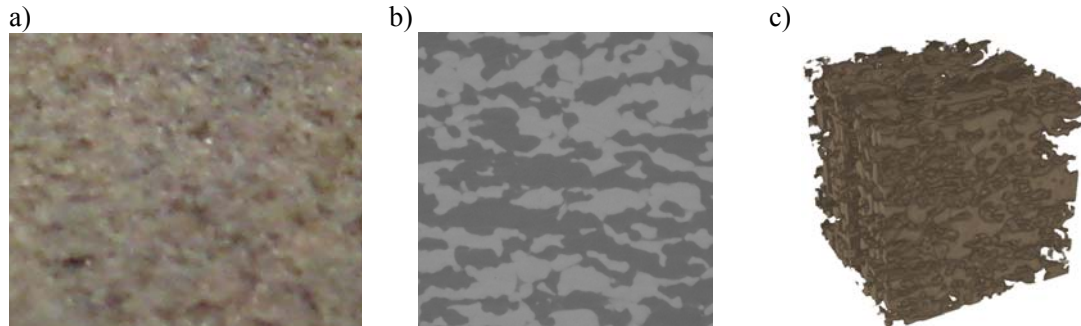
a)   b)   c)

Fig. 4. Photo (a), CT image (b), and 3D rendering of the ceria foam sample.

CT-based calculations show enhanced extinction in z-direction because of squeezed pores resulting in shorter attenuation paths. k_e in the x- and y-directions increase due to the more parallel alignment of the structures with the heat flux in these directions. h_e in z-direction is larger because of the more tortuous path for fluid flow, increasing the accessible surface area for fluid-solid heat exchange. Reduced K and larger F_{DF} in z-direction are observed because of larger tortuosity along this direction.

Studies on tailored foam designs, adjusted to the specific needs of the process in which the foam is applied, allow for foam engineering and consequently enhanced process performance.

5. Conclusions and outlook

This paper examined complex, chemically reacting multi-phase media used in high-temperature solar energy applications. The reliable determination of the morphological and effective heat/mass transfer properties, based on the exact morphology obtained by computed tomography, were presented for three examples of porous materials employed in solar processes for power generation and fuel generation.

The CT-based multi-scale methodology enables in-depth understanding and reliable process modeling, which are required for optimization. Other energy-related fields of applications are insulation porous materials; enhanced electrodes and electrolytes for fuel cells; and semiconductors for thermoelectrical devices.

References

[1] Steinfeld, A., and Meier, A., 2004, Solar fuels and materials, Encyclopedia of Energy, 5, pp. 623-637.

[2] Whitaker, S., 1999, The method of volume averaging, theory and applications of transport in porous media, Kluwer Academic Publisher, Dordrecht.

[3] Loretz, M., Coquard, R., Baillis, D., and Maire, 2009, Metallic foams: Radiative properties/comparison between different models, Journal of Quantitative Spectroscopy and Radiative Transfer, 109, pp. 16-27.

[4] Fu, X., Viskanta, R., and Gore, J., 1997, A model for the volumetric radiation characteristics of cellular ceramics, International Communication on Heat and Mass Transfer, 24, pp. 1069-1082.

[5] Tancrez, M., and Taine, J., 2004, Direct identification of absorption and scattering coefficients and phase function of a porous medium by a Monte Carlo technique, International Journal of Heat Transfer, 47, pp.373-383.

[6]   Petrasch, J., Wyss, P., and Steinfeld, 2007, Tomography-based Monte Carlo determination of radiative properties of reticulate porous cermaics, Jorunal of Quantitative Spectroscopy and Radiative Transfer, 105, pp. 180-197.

[7]   Haussener, S., Lipiński, W., Petrasch, J., Wyss, P., and Steinfeld, A., 2009, Tomographic characterization of a semitransparent-particle packed bed and determination of ist thermal radiative properties, Journal of Heat Transfer, 131, 072701.

[8]   Boomsma, K., and Poulikakos, D., 2001, On the effective thermal conductivity of three-diemnsionally structure fluid-saturated metal foam, International Journal of Heat and Mass Transfer, 44, pp. 827-836.

[9]   Bhattacharya, A., Calmidi, V., and Mahajan, R., 2001, Thermophysical properties of high porosity metal foams, Internaional Journal of Heat and Mass Transfer, 45, pp. 1017-1031.

[10] Fu, X., Viskanta, R., and Gore, J., 1998, Prediction of effective thermal conductivity of cellular ceramics, International Communication on Heat and Mass Transfer, 25, pp. 151-160.

[11] Kaviany, M., 1999, Principles of heat and mass transfer in porous media, Springer, New York.

[12] Coray, P., Lipiński, W., and Steinfeld, A., 2010, Experimental and numerical determination of thermal radiative properties of ZnO particulate media. Journal of Heat Transfer, 132, 012701.

[13] Haussener, S., Coray, P., Lipiński, W., Wyss, P., and Steinfeld, A., 2010, Tomography-based heat and mass transfer characterization of reticulate porous ceraimcs for high-temperature processing, Journal of Heat Transfer, 132, 023305.

[14] Osinga, T., Lipiński, W., Guillot, E., Olalde, G., and Steinfeld, A., 2006, Experimental Heat Transfer, 19, pp. 69-79.

[15] Calmidi, V., and Mahajan, R., 1999, The effective thermal conductivity of high porosity fibrous metal foams, Journal of heat transfer, 121(2), pp. 466–471.

[16] Younis, L., and Viskanta, R., 1993, Experimental determination of the volumetric heat transfer coefficient between stream of air and ceramic foam, International Journal of Heat and Mass Transfer, 36(6), pp. 1425–1434.

[17] Gnielinski, V., 1978, Gleichung zur Berechnung des Wärme- und Stoffaustausches in durchströmten ruhenden Kugelschüttungen bei mittleren und grossen Pecletzahlen, Verfahrenstechnik, 12, pp. 363-366.

[18] Saidi, M., Rasouli, F., and Hajaligol, M., 2006, Heat transfer coefficient for a packed bed of shredded material at low Peclet numbers, Heat Transfer Engineering, 27, pp. 41-49.

[19] Kaviany, M., 1995, Principles of Heat Transfer in Porous Media, Springer.

[20] Ergun, S., 1952, Fluid flow through packed beds, Chem. Eng. Prog, 48(2), pp. 81-96.

[21] Petrasch, J., 2006, Tomography-based Methods for Reactive Flows in Porous Media: Applied to Solar Thermal Reforming of Hydrocarbons, VDM.

[22] Haussener, S., 2010, Tomography-based determination of effective heat and mass transport properties of complex multi-phase media, PhD thesis, ETH Zurich.

[23] Berryman, J., and Blair, S., 1986, Use of digital image analysis to estimate fluid permeability of porous media; Application of two-point correlation functions, Journal of Applied Physics, 60, pp. 1930-1938.

[24] Lipiński, W., Keene, D., Haussener, S., and Petrasch, J., 2010, Continuum radiative heat transfer modeling in media consisting of optically distinct components in the limit of geometrical optics, Journal of Quantitative Spectroscopy and Radiative Transfer, 111, pp. 2474-2480.

[25] Haussener, S., Lipiński, W., Petrasch, J., Wyss, P., and Steinfeld, A., 2009, Tomographic characterization of a semi-transparent-particle packed bed and determination of its thermal radiative properties, Journal of Heat Transfer, 131, 072701.

[26] Whitaker, S., 1996, The Forchheimer equation: Atheoretical development, Transport in Porous Media, 25, pp. 27-61.

[27] Coquard, R., and Baillis, D., 2005, Radiative characteristics of beds of spheries containing an absorbing and scattering medium, Journal of Thermophysics and Heat Transfer, 19, pp. 226-234.

[28] Delisée, C., Lux, J., and Malvestio, J., 2009, 3D morphology and permeability of highly porous cellulosic fibrous material, Transport in Porous Meida, 91, pp. 623-636.

[29] Piller, M., Schena, G., Nolich, M., Favretto, S., Radaelli, F., and Rossi, E., 2009, nalysis of hydraulic permeability in porous media: From high resolution X-ray tomography to direct numerical simulations, Transport in Porous Media, 80, pp. 57-78.

[30] Mecke, K., and Stoyan, D., 2002, Morphology of condensed matter, Springer, Berlin.

[31] Trommer, D., Noembrini, F., Fasciana, M., Rodriguez, D., Morales, A., Romero, M., and Steinfeld, A., 2005, Hydrogen production by steam gasification of petroleum coke using concentrated solar power – I. Thermodynamic and kinetic analysis, International Journal of Hydrogen Energy, 30, pp. 605-618.

[32] Piatkowski, N., and Steinfeld, A., 2008, Solar-driven coal gasification in a thermally irradiated packed-bed reactor, Energy and Fuels, 22, pp. 2043-2052.

[33] Chueh, W., Falter, C., Abbott, M,, Scipio, D., Furler, P., Haile, S., and Steinfeld, A., 2010, High-Flux Solar-Driven Thermochemical Dissociation of CO_2 and H_2O using Nonstoichiometric Ceria, Science, 330, pp. 1797-1801.